Influence of liquid hydrophobicity and nozzle passage curvature on microfluidic dynamics in a drop ejection process

Jr-Ming Lai[1], Chang-Yan Huang[1], Chih-Hao Chen[1], Kung Linliu[2] and Jenn-Der Lin[1]

[1] Department of Mechanical Engineering, National Chiao Tung University, 1001 Ta Hsueh Road, Hsinchu 30050, Taiwan, Republic of China
[2] Scientific Research/Facility Utilization, National Synchrotron Radiation Research Center, 101 Hsin-Ann Road, Hsinchu Science Park, Hsinchu 30076, Taiwan, Republic of China

E-mail: jdlin@cc.nctu.edu.tw and klinliu@nsrrc.org.tw

Abstract
Employing methods of computational fluid dynamics, we investigated the physical phenomena and fluid dynamics of a microfluid during ejection of a droplet with a designed system of a nozzle plate connected to a flat-plate piezoelectric material. A comparison between experimental measurements and numerical simulations was devised to validate the theoretical model. The volume-of-fluid piecewise linear-interface construction (VOF-PLIC) interface-capturing method was adapted to represent the fluid domain and to track the evolution of its free boundaries whereas the continuous surface force (CSF) mode was chosen to model the interfacial physics. The results show that the curvature of the flow channel affects the velocity, period before disintegration, volume of the droplet and number of satellite drops. Increasing the diameter of the orifice increases the volume and decreases the velocity of the droplet. Increasing the amplitude or frequency of the nozzle plate raises the input energy, so increasing the velocity, decreasing the volume and hastening the disintegration of the droplet, but an increased amplitude or frequency increases the number of satellite drops. At the hydrophobic boundary, the velocity increases, the droplet volume decreases and the period before disintegration is abbreviated because of the decreased adhesive force between the fluid and the boundary surface.

(Some figures in this article are in colour only in the electronic version)

1. Introduction

New fabrications of oligonucleotide microarrays (Dijksman and Pierik 2008), color filters for liquid-crystal display panels (Kim *et al* 2009), multicolor polymer light-emitting diode displays (Shimoda *et al* 2003), visualization of protein distribution (Komatsu *et al* 2008) and transistors (Ridley *et al* 1999) have warranted increasing attention to ink-jet printing. Ink-jet print heads are of two main types—continuous ink jets (CIJ) and drop-on-demand (DOD) ink jets. In the CIJ print head, sufficient pressure applied to the ink supply causes liquid to emerge continuously from a nozzle to form a jet, which disintegrates into a train of drops through Rayleigh instability

(Rayleigh 1878). In contrast, the liquid remains in a DOD print-head nozzle, forming a meniscus unless induced pressure is applied to overcome the surface-tension forces (Pond 2000). Because of its simplicity and the feasibility of decreasing the size of the system, the DOD ink-jet print head has a major share of the market for ink-jet printers.

The basic configuration of an ink-jet print head is typically composed of a chamber with one open end, called a nozzle, from which a liquid jet emanates to disintegrate into droplets; the other end is connected to a fluid reservoir that supplies the liquid to produce the next drop. Most commercial DOD ink-jet printers use either a thermal or a piezoelectric method to convert an electrical signal into the motion of the

fluid (Pond 2000). In the thermal ink-jet print head, the expansion of a bubble of vapor, induced with an electrically operated miniature heater, forces the fluid into motion. The piezoelectric ink-jet print heads substitute the deformation of an electrically actuated solid sheet to expand the bubble (Allen *et al* 1985, Pond 2000). To actuate the piezoelectric material or the heating element, an excitation signal, generally a pulse, is required to be incorporated. The advantage of the thermal ink-jet print head is that it can be produced with a micro electro-mechanical system (MEMS), but its great disadvantage is its short lifetime (Pond 2000, Le 1998). Moreover, liquid in the thermal print head must be heated and vaporized to form a bubble as a pump. This heating might cause chemical modification of the properties of the liquid and thereby limit the application of this print head. The piezoelectric ink-jet print head is extensively exploited for its reliability and adaptability in various applications of micro-fluidic control, even though the means of production and a large driven-voltage pulse entail great cost. The quality of ink-jet printing is closely correlated with the jet performance in forming a drop, which is dominated by viscous, capillary and inertial forces.

To further improve these ink-jet print heads, the phenomena involved in forming a drop should be fully understood. Many experimenters have visualized the liquid jet and drop formation from DOD ink-jet print heads (Chen *et al* 1997, Fan *et al* 2008, Kwon 2009, Meinhart and Zhang 2000, Shield *et al* 1987); for instance, Meinhart and Zhang (2000) utilized a particle-image velocimetry system with micrometer resolution to measure simultaneously the velocity flow field, with spatial resolution up to 5–10 μm and temporal resolution up to 2–5 μs. Fan *et al* (2008) assessed the drop quality from a temporal sequence of magnified images recorded with a charge-coupled print head (CCD) camera along and a stroboscopic technique when varying the nozzle sizes, voltage signals and liquid properties. Kwon (2009) developed a technique for edge detection for the jetting speed and drop diameter using CCD camera images with varied trigger times.

The prediction of the formation of a droplet, which can not only validate theoretical models with experimental observations but also provide insight into asymptotic conditions, challenges numerical simulation. Early models failed to predict the temporal evolution of the drop velocity, shape and trajectory through inadequate models of interfacial physics and complicated topology changes (Asai 1992, Asai *et al* 1987, Chen *et al* 1999, Fromm 1984, Pimbley 1976). As a consequence of the evolution of numerical methods and increased computing power, computational fluid dynamics (CFD) has become a promising tool to overcome the limitations of theoretical models. Among diverse approaches, the volume-of-fluid (VOF) method proposed by Hirt and Nichols (1981) has proved effective and successful for its simplicity and robustness (Feng 2002, Link and Semiat 2009, Liou *et al* 2002, Moon *et al* 2008, Pan *et al* 2002, Wu *et al* 2004, Yang *et al* 2006). Wu *et al* (2004) demonstrated the feasibility of the full cycle of ink-jet printing process including drop ejection, drop formation and drop collision against a target substrate by developing their own simulation system;

this system, employing a method based on finite differencing to solve the fluid dynamics and the VOF method to capture the interface change, was validated with experimental observation. Liou *et al* (2002) simulated the ejection of a SEAJet print head on applying commercial CFD software (COMET, StarCD Suite) based on the VOF method to treat free-surface problems. COMET discretizes governing equations with a finite-volume approach and exploits the continuous surface force (CSF) model to account for the surface tension effect. In this paper, the predicted evolution of the meniscus inside the print head was compared with the experimental results in the literature. Pan *et al* (2002) used Flow-3D (commercial CFD software) to simulate the formation of drops from a micro-electro-mechanical diaphragm drop ejector (MEMSJet) and provided useful information concerning the design of this print head; the ejection mechanism of the MEMSJet is that when a bias voltage is applied between a diaphragm and counter electrode, the diaphragm is deflected, therefore causing the volume variation of ink chamber to discharge liquid. Flow-3D used in that study is capable of modeling the free-surface problems, employing the finite-volume approach to solve the governing equations of fluid flow and the VOF method to track effectively the interface deformations. Feng (2002) conducted various numerical experiments to find some design rules of ink-jet print heads utilizing the same software, Flow-3D. In this work, volume, velocity and shape of drops were chosen to evaluate the jetting performance. Yang *et al* (2006) exploited CFD software, CFD-ACE+, also applying the VOF approach for interface tracking to explore numerically the drop ejection of a Picojet print head. In this research, 17 simulation cases were performed to reveal the design concept of this print head. Anantharamaiah *et al* (2007) employed the CFD code from Fluent Inc. to investigate the relationship between the nozzle inlet roundness and the diameter of an ejected liquid jet in the applications of hydroentangling. The interfacial flow model used in this study was the VOF method along with the CSF model to consider the surface tension effect. The paper of Anantharamaiah *et al* (2006) provides extensive discussions of the effect of nozzle geometry on the formation of constricted waterjets, which have an air gap between the liquid and nozzle wall. In this study, the VOF method together with the CSF model was used as the two-phase flow model. Although other numerical methods have been proposed (Suh and Son 2008, Yu *et al* 2005), the VOF methods are still considered as the commonly used methods to model the drop formation in DOD ink-jet print heads.

As the above literature review shows, most previous workers focused on the influence of the ink-jet print head geometry, the diameter of the nozzle exit, amplitude and frequency of electrically driven signals, and liquid properties, density, viscosity and surface tension on the drop formation, but little is known about the effect of the wetting condition of the nozzle wall and its curvature on the drop formation through the ink-jet print heads. Furthermore, when an ink-jet print head is fabricated in progressively smaller size for the purpose of enhancing resolution, the capillary effects including the vapor–liquid interfacial tension and the wetting condition on the solid wall, coupled with curvature of that wall, play an
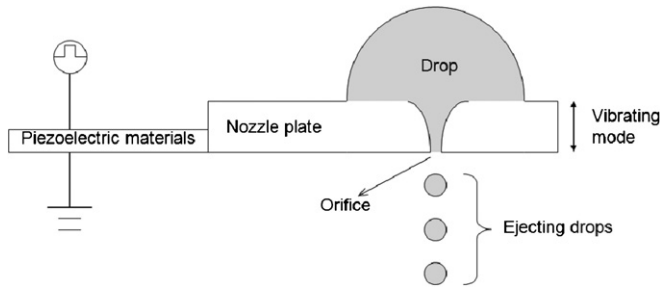
Figure 1. Diagram of a nozzle-plate system.

increasingly important role on the drop ejection. In the present work, we performed numerical simulations to investigate the detailed process of the formation of a droplet when considering various dynamic contact angles (various dynamic contact-angle patterns represent varied wetting conditions) and curvature of the nozzle wall. To simplify the models stemming from the complicated geometry of the interior flow channels in ink-jet print heads, we adopted a model of a nozzle plate connected with a flat-plate piezoelectric material; we compared the numerical results with experimental measurements to validate the present computer code. The results of this work might provide suggestions about the design of ink-jet print heads and improve our understanding of the formation of a droplet.

2. Theoretical models and solution methods

Consider a system of a nozzle plate joined to a flat-plate piezoelectric material having a liquid drop on it as shown in figure 1.

When a voltage signal is applied to the piezoelectric material, it alters its dimensions periodically, therefore inducing an acoustic wave to propagate through the nozzle plate and the liquid drop. This propagation of the acoustic wave causes a vibrational motion of the nozzle plate and an oscillating pressure difference between the liquid and the air, thus driving drops to become ejected. Our objective is to observe the influence of the exit diameter of the nozzle, the curvature of the nozzle passage, the wetting conditions of the nozzle passage wall and the vibration of the nozzle plate on the variables of immediate practical importance such as the drop volume, the speed and the pinching-off time during the drop formation. Shown in figure 2 is the configuration adopted in our theoretical models and simplified to be axially symmetric in terms of the reality of the experimental arrangement.

Here, we consider a hemispherical liquid drop placed on a flat solid wall drilled for liquid protrusion and moving up and down in a specific fashion corresponding to the vibration of the realistic nozzle plate, thus causing a pressure difference between the liquid and the ambient atmosphere so as to expel the liquid drops. According to Feng (2002), the assumption that the fluid is incompressible is acceptable, as the propagation wavelength which is estimated to be 7500 μm is greater than the radius of the hemispherical liquid drop which is 4000 μm. In the current estimate of the propagation wavelength, the speed of the propagation of the acoustic wave in water is approximately 1500 m s^{-1} and the frequency of the acoustic wave is set to 200 kHz used in the present study. Thus the dynamics of drop formation is governed by the Navier–Stokes equation and the continuity equation for incompressible fluid that obeys the linear Newtonian friction law as follows:

$$\nabla \cdot \overrightarrow{V} = 0, \tag{1}$$

$$\frac{\partial}{\partial t}(\rho \overrightarrow{V}) + \rho(\overrightarrow{V} \cdot \nabla)\overrightarrow{V} = -\nabla p + \rho \overrightarrow{g} + \mu \nabla^2 \overrightarrow{V} + \overrightarrow{F}_s, \tag{2}$$
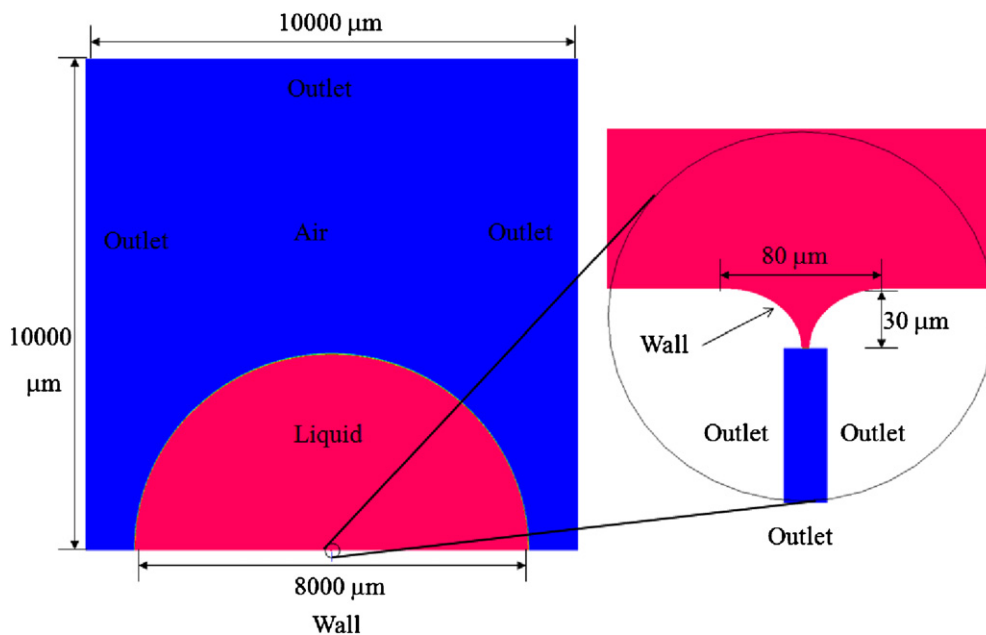

Figure 2. Configuration of the computational domain.

where t is the time, $\vec{V}$ is the velocity vector, p is the mean pressure, μ is the viscosity, ρ is the density, $\vec{g}$ is the gravitational acceleration and ∇ is the gradient operator. Here, $\vec{F_s}$, derived from the CSF mode (Brackbill *et al* 1992) that translates surface tension into a continuous effect across an interface rather than a boundary condition on the interface, represents an interfacial surface tension term as

$$\vec{F_s} = \vec{f_\sigma}\delta_\sigma, \tag{3}$$

where $\vec{f_\sigma}$ is the surface tension force per unit interfacial area and δ_σ is a surface delta function restricting the surface tension force $\vec{F_s}$ being applied in the minute bounded region containing the interface.

In modeling this drop formation phenomenon, it is important to describe accurately the free surface in a mathematical form that can treat robustly the interfacial change with a complicated topology. Here, we adopt an interface-capturing method, a variation of the VOF scheme, to resolve this transient behavior of the free surface separating two incompressible and immiscible fluids. The principle of the VOF-based free-surface-capturing method is to define a volume fraction variable C as a ratio of volume occupied by a liquid in a computational cell to the total cell volume; by definition, variable C takes the value 1 at the liquid side and 0 at the air side. The transitional region ($0 < C < 1$) depicts the free surface, the position of which is generally defined as the value $C = 0.5$. Under a consideration of conserved mass, we derive the evolution equation of variable C as follows (Rider and Kothe 1998, Kothe *et al* 1996):

$$\frac{\partial C}{\partial t} + (\vec{V} \cdot \nabla)C = 0. \tag{4}$$

Based on the VOF method, the volumetric force $\vec{F_s}$ associated with surface tension can be represented as follows (Brackbill *et al* 1992):

$$\vec{F_s} = \sigma\left[-\nabla \cdot \left(\frac{\nabla C}{|\nabla C|}\right)\right]\nabla C, \tag{5}$$

where σ is the surface tension and the term in brackets describes the mean curvature of the free surface. The critical issue in this free-surface-capturing method is the discretization of the convective term in equation (4). Here, we use in particular a multidimensional upsplit advection algorithm with a piecewise linear-interface construction (PLIC) scheme to discretize this convective term (Rider and Kothe 1998).

The spirit of this free-surface-capturing method is to regard two fluids as a single effective fluid and that both two fluids share the same velocity field. When the velocity variables are worked out from equations (1) and (2), and then substituted into equation (4), the new volume fraction C value in the next time step becomes updated on solving equation (4); equation (4) must hence be coupled with equations (1) and (2) to obtain the redistribution of variable C in the next period. The physical properties of the effective fluid including the density and viscosity in each computational cell are determined in the following manner:

$$\rho_e = C\rho_L + (1 - C)\rho_G, \tag{6}$$

$$\mu_e = \frac{C\rho_L\mu_L + (1 - C)\rho_G\mu_G}{\rho_e}, \tag{7}$$

where the subscripts L and G denote the liquid and gaseous phases, respectively.

For the model considered here, the arrangement of the types of boundary condition is shown in figure 2. The wall boundary meets the following conditions:

$$\vec{V} \cdot \vec{n}_{\text{wall}} = 0, \tag{8}$$

$$\vec{V} \cdot \vec{t}_{\text{wall}} = 0, \tag{9}$$

$$\frac{\partial p}{\partial \vec{n}_{\text{wall}}} = 0, \tag{10}$$

where $\vec{n}_{\text{wall}}$ and $\vec{t}_{\text{wall}}$ represent outward normal and tangential vectors for the wall, respectively. Apart from the boundary conditions above, the problems with free surface flow require also the conditions at the moving contact line, defined as a location at which liquid, gaseous and solid phases meet, to be specified for a variable level of the wettability of the nozzle wall. In treatment of this wetting condition, we assume that the contact angle, formed by the liquid/gas and liquid/solid interface, equals the static (equilibrium) angle according to Young's equation:

$$\sigma \cos\theta_e = \sigma_{sg} - \sigma_{sl}, \tag{11}$$

where θ_e is the static contact angle and σ, σ_{sg} and σ_{sl} are liquid/gas, solid/gas and solid/liquid interfacial forces, respectively; the related dynamic contact angle on the wall regions is hence set constant during the drop formation. The implementation of the boundary condition for the dynamic contact angle is readily incorporated within the framework of the CSF model. Volumetric force $\vec{F_s}$ applied to the numerical cells immediately at the solid walls is calculated with

$$\frac{\nabla C}{|\nabla C|} = \vec{n}_{\text{wall}}\cos\theta_e + \vec{t}_{\text{wall}}\sin\theta_e. \tag{12}$$

To model appropriately the vibration of the nozzle plate, we assume that the instantaneous displacement of the solid wall boundaries adopts a trigonometric form,

$$D = A \cdot \sin(2\pi f t), \tag{13}$$

where A is the displacement and f is the frequency. At the outlet boundary, the conditions are satisfied as follows:

$$p = \text{constant}, \tag{14}$$

$$\frac{\partial \vec{V}}{\partial \vec{n}_{\text{out}}} = 0, \tag{15}$$

$$C = 0. \tag{16}$$

Here, $\vec{n}_{\text{out}}$ signifies an outward normal vector on the boundary paths. In addition, the pressure and velocity inside fluids are initially 1 atm and at rest, respectively. The initial distribution of liquid and gaseous materials is shown in figure 2. All computations were performed with commercial software CFD-ACE+ for CFD, which is a multipurpose computer code based on finite-volume discretization to solve the two-dimensional axially symmetric Navier–Stokes and
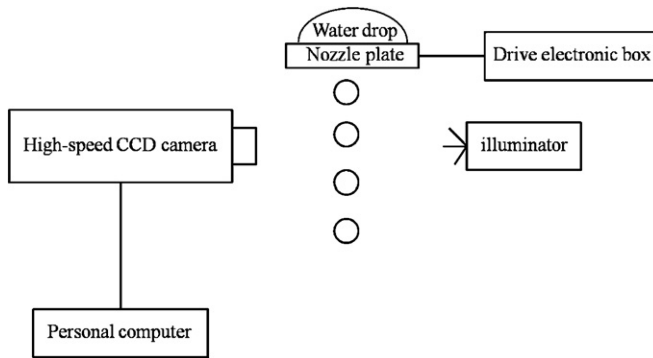
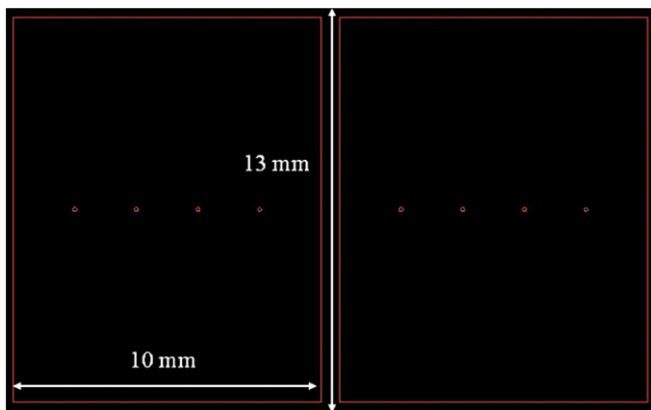**Figure 3.** Schematic diagram of the experimental setup.

Figure 4. Mask pattern used to fabricate a nozzle plate.

continuity equations for the velocity and pressure variables. The velocity–pressure coupling was conducted with an iterative semi-implicit method for pressure-linked equations in a consistent (SIMPLIC) numerical scheme. The velocity and pressure fields in a time step were obtained when the convergence criteria are satisfied. In addition, the specified displacement, given by equation (13), was programmed as a customized user subroutine with a prescribed moving boundary condition, which is compatible with the CFD-ACE+ computer code.

3. Experimental methods and conditions

In order to validate the theoretical models as mentioned above, we used high-speed photography for visualizing the droplet formation process and utilized the experimental setup shown schematically in figure 3. In the present experiments, droplets are expelled from a nozzle plate connected with a flat-plate piezoelectric material, as shown in figure 1. To circumvent the difficulty of flow visualization and crosstalk of ejected droplets, we placed the nozzles in a row with a hole-to-hole spacing of 2 mm on the nozzle plate, which is 10 mm in length and 13 mm in width, as shown in figure 4 and fabricated by lithography and electroforming (Chen *et al* 2005, Cheng *et al* 2005, Ehrfeld 2002).

Figure 5 shows the schematic diagram of the process of fabricating the nozzle plate. The mold patterning and the

nickel electroforming were the main process to construct the nozzle plate used in this study. A silicon wafer coated with aurum having a 100 nm thickness was used as a substrate for constructing the electroforming components. The positive tone photoresist (AZ 1500) was used as electroforming molds and nickel was the electroforming material. The mechanism of forming a nozzle in a substrate was by over-electroforming around the columnar photoresist mold. When the thickness of deposited nickel material is larger than the height of the columnar mold, the deposited nickel begins to develop laterally and vertically. The greater the over-electroforming, the smaller the nozzle orifice becomes. Therefore, a nozzle with an ellipsoid-like curvature of passage could be produced. Figure 6 shows the SEM photo of a nozzle used in this study. The conductive epoxy adhesive was applied on the attached interface between the nozzle plate and the piezoelectric material, which is 24 mm in length, 18 mm in width and 0.7 mm in thickness. Moreover, the field of this attached interface is 1 mm in length and 13 mm in width. If the periodic voltage signal whose waveform was square, peak-to-peak amplitude 24 V and frequency 63.3 kHz were applied to the piezoelectric material, the nozzle plate would vibrate periodically, which is induced by the deformation of piezoelectric material along with constraint on one edge opposite to the nozzle plate, as shown in figure 7. As mentioned above, the realistic nozzle configuration is approximately axisymmetric to the nozzle center line through the fabrication of lithography and electroforming, as presented in figure 6. In the present experiment, the gravitational force is directed toward the direction of nozzle center line and the interference of ejected droplets in different nozzles can be ignored due to the large hole-to-hole spacing of up to 2 mm compared to drop size. Moreover, the diameter of nozzle inlet and nozzle outlet is small enough compared to the size of the nozzle plate and hemispherical liquid drop on the nozzle plate, so the vibration mode near the nozzle region can be simply assumed to move up and down along the direction of nozzle center line.

The micro-flow visualization system consists of a charge-coupled device (IDT XS-4) equipped with a long distance microscope including a 6.5× optical system (Optem zoom-125) and a 5× objective lens (Mitutoyo 378-803-2). A high intensity illuminator (Techniquip FOI-250) with 250 W was used as a light source. The camera can capture images at a limited rate of 73 500 frames per second due to the constraint of an observed field where the formation of droplet occurs. In the present study, the limited capturing rate of images is insufficient for observing the detailed process of drop breakup; however macro features of drop formation including drop volume and drop flight speed could be determined from the sequence of liquid ejection images and compared with theoretical models. The images were then processed by an image acquisition card, displayed on the screen of a monitor and stored in a personal computer as files. Moreover, the image of a well-defined scale is also examined and captured through the CCD camera with the same magnification of the microscope used to observe the drop ejection process. With the aid of image processing software (ImageJ 1.42), the number
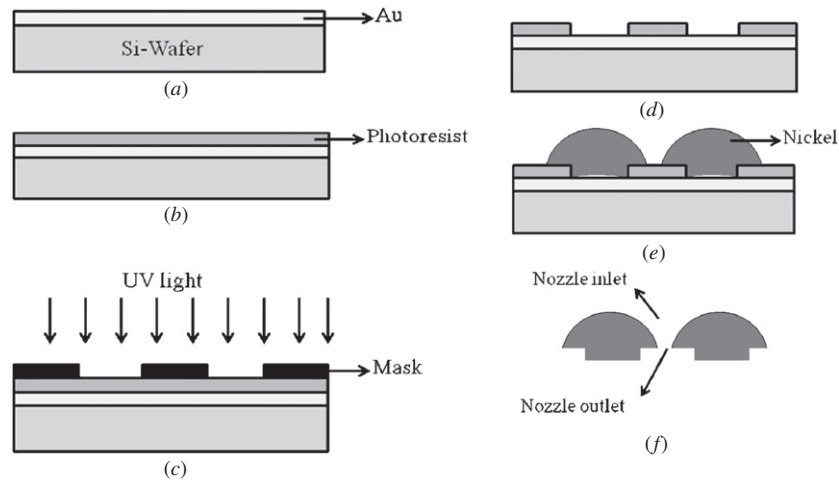
Figure 5. Schematic diagram of the process of fabricating a nozzle plate: (*a*) metal deposition, (*b*) resist coating, (*c*) UV light exposure, (*d*) pattern development, (*e*) electroforming and (*f*) take off.
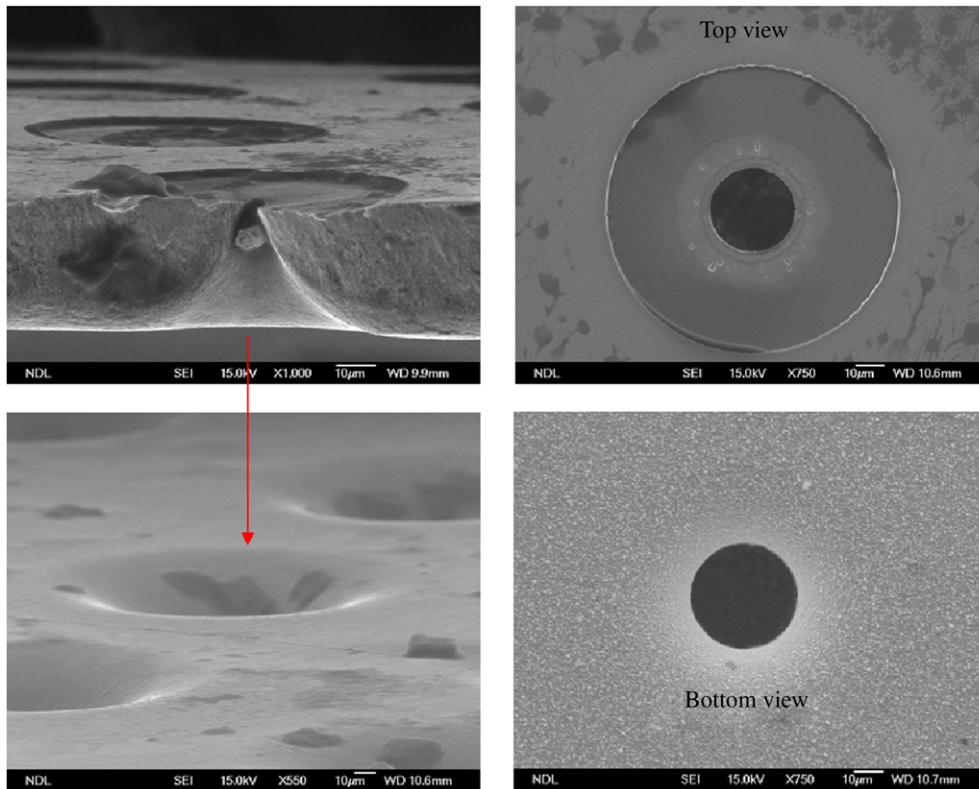

Figure 6. SEM photo of a fabricated nozzle.

of pixels per micrometer can be obtained and the reciprocal of this quantity represents the spatial resolution defined as a length per pixel. Based on the spatial resolution defined, the length of target line is calculated by measuring the number of pixels this line holds.

With de-ionized water as the working fluid whose volume was fixed at 100 μL and placed on the center of the nozzle plate, the shape of the ejected droplet after the oscillation of the surface wave was sufficiently decayed by viscous dissipation could be approximated to a sphere whose diameter was determined by measuring the maximum end-to-end distance

of the liquid drop on the monitor screen and could be used to estimate the drop volume. In addition, the drop velocity was determined by measuring the displacement of the leading edge of the droplet in a time period, as shown in figure 8. The uncertainty in the measurement of the length is around ± 3 μm, which could be attributed to the limit of the observed scope and spatial resolution of the camera associated with exposure time.

In order to measure the wetting condition of the system, we simply placed a hemispherical water drop on the nozzle plate. The visualization method mentioned above also allows
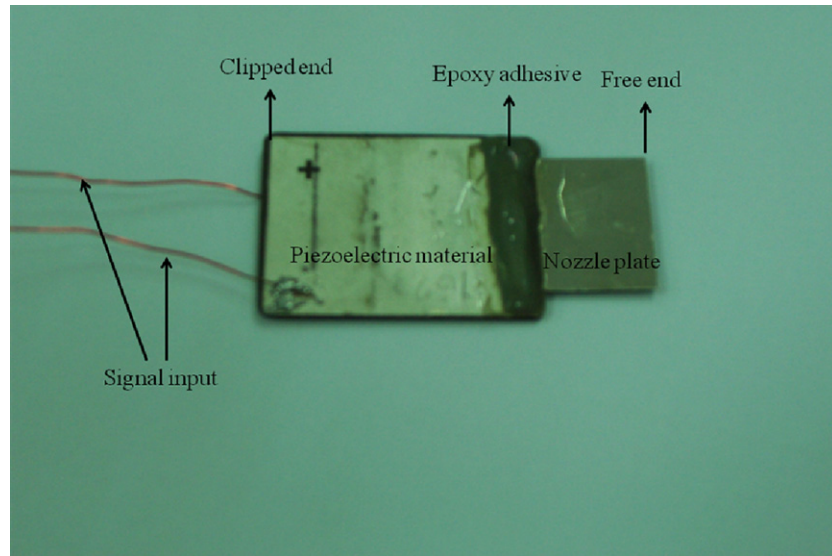
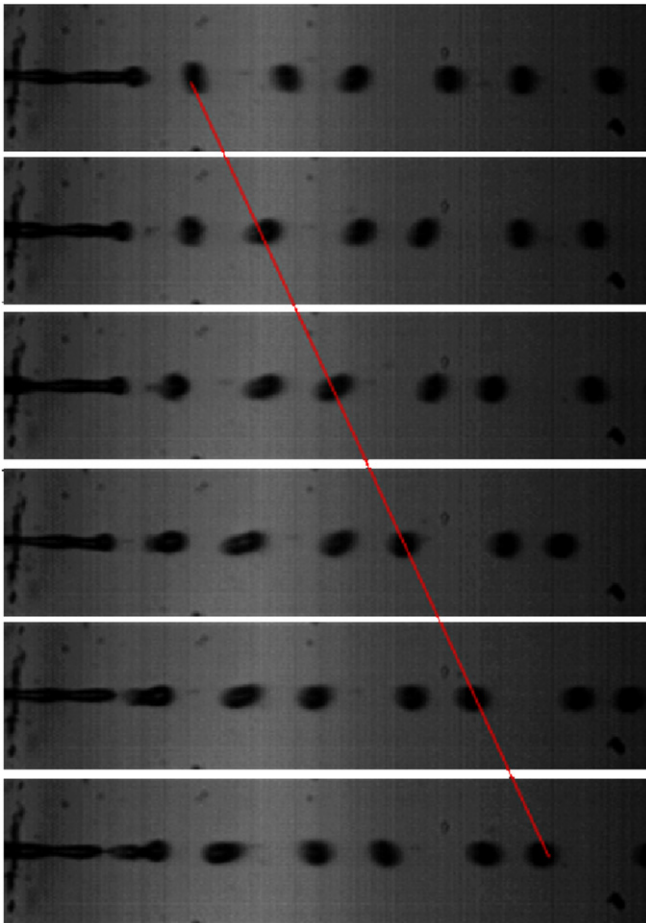**Figure 7.** Picture of the nozzle plate connected with piezoelectric material.

Figure 8. Measurement of droplet velocity using the time sequence of the ejected liquid drop; the solid line indicates the same droplet in different time periods.

a measurement of the contact angle, which is defined as an angle between the tangent to the drop profile and tangent to the surface at the intersection point of air, liquid and solid,

and represents the wetting condition of the considered system. The difficulty was in the accurate estimate of the tangent to the curved drop profile since the end point of this curve must be measured. Moreover, this visualization method also requires that the drop be in focus and the base line tangent to the liquid–solid interface is sufficiently clear. All measurements of the contact angle can be done by directly using image processing software (ImageJ 1.42). The contact angle of nickel material was measured to be 73°, as shown in figure 9(*a*). By conducting reactive ion etching (RIE), we can shift the contact angle of the nickel nozzle plate from 73° to 54° due to the change in surface roughness, as shown in figure 9(*b*).

4. Results and discussion

4.1. Model validation

In an early stage of this work, we performed tests of the grid dependence with the total number of grids being about 175 432, 195 388 and 251 496. As shown in figure 10, the computational domain having the shape of a cylindrical pie slice uses 2D axially symmetric grids, thus enabling 2D computations in a cylindrical coordinate system. To achieve a uniform distribution of the discretization errors, we utilized non-uniform grids that adopt small grid spacing in regions such as near the nozzle, the immediate solid walls and the trajectory of the flight drops for which the derivatives of the variables alter rapidly and large discretization errors are expected. The solution domain above the nozzle plate represents a large square 5×10 mm^2 in the r–z plane, which contains the quadrant liquid drop of radius 4 mm. In the nozzle region, the variation of the curvature of the nozzle passage approximates an elliptic shape. All other parameters are listed in table 1. Here, R_{exit} is the radius of the nozzle exit, $R_{entrance}$ is the radius of the nozzle entrance, T is the thickness of the nozzle plate, A is the vibration amplitude of the nozzle plate, f is the vibration frequency of the nozzle plate and θ_e is the static contact angle of the nozzle passage wall. With water
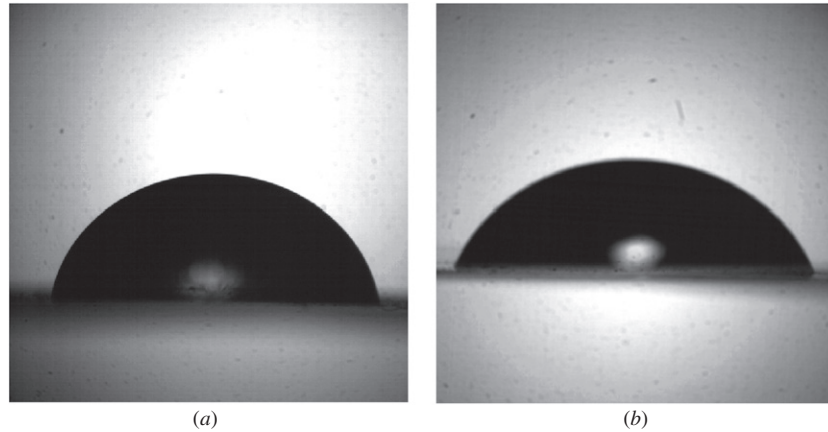
Figure 9. Measurement of the contact angle using the visualization method: (*a*) water drop on the nickel surface and (*b*) water drop on the nickel surface processed by RIE.
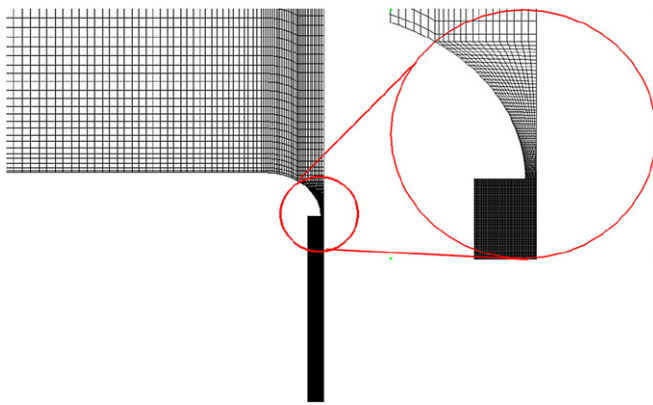

Figure 10. Magnified view of numerical grids neighboring the nozzle exit.

Table 1. Parameters for the grid dependence test.

R_{exit} (μm)	$R_{entrance}$ (μm)	T (μm)	A (μm)	f (kHz)	θ_e (deg)
2	40	30	0.25	100	7.1

Table 2. Parameters for the validation cases.

Case	R_{exit} (μm)	$R_{entrance}$ (μm)	T (μm)	A (μm)	f (kHz)	θ_e (deg)
A	17	55.75	46	0.275	61.703	73
B	22.35	60.35	46	0.341 24	64.63	54

as a working fluid, the mass density, viscosity and surface tension are 10^3 kg m^{-1}, 1.0×10^{-3} N s m^{-2} and 7.27×10^{-2} N m^{-1}, respectively. All these parameters are consistent with the experimental measurements. To obtain the velocity and pressure fields in a time step, we required that the normalized residual errors of flow variables converge to 10^{-4}. The entire simulation required 456 h (CPU time on a computer with a Pentium P4 processor at 3.0 GHz). The grid convergence study shows that the average drop velocity and drop volume with 175 432 grids were 20.45 m s^{-1} and 0.045 pL, while those with 195 388 grids were 20.5 m s^{-1} and 0.0442 pL, respectively. Moreover, the average drop velocity and drop volume with 251 496 grids were 20.9 m s^{-1} and 0.044 pL, respectively. These tests indicate that the 175 432 grids were sufficiently fine, causing an estimated discretization error smaller than 3% and achieving a compromise between accuracy and CPU time. In this study, a simulation case was also carried out to demonstrate the repeatability of the prediction of the drop formation process not shown here.

To validate the present theoretical models, we also made a comparison between numerical calculations and experimental results. Table 2 offers the parameters used. Figure 11 shows a qualitative comparison of the prediction with the visualized micro-image of the liquid shape at a time instant.

Both experimental and numerical results showed that the liquid column was ejected continuously in these circumstances even if the driving force imposing momentum on the liquid drop and induced by the vibration of the nozzle plate varied periodically.

A quantitative comparison shows that, in case A, the measured volume and average velocity of each formed drop consistently were 22.812 pL and 4.3 m s^{-1}, respectively, whereas the predicted volume and average velocity were 22.657 pL and 4.173 m s^{-1}, respectively. For case B, the measured volume and average velocity were 43.009 pL and 6.27 m s^{-1}, respectively, whereas the predicted volume and average velocity were 44.16 pL and 6.52 m s^{-1}, respectively. Here, the shape of the liquid drop is approximated as spherical from the pinching-off point and the average velocity was estimated on measuring the distance of the drop flight over an interval of 10 μs in both numerical and experimental results. The errors between measured and predicted average velocities are thus 2.9% for case A and 4.0% for case B, and the errors of drop volume are 0.68% for case A and 2.7% for case B. In general, the predicted results involving both quantitative and qualitative aspects agree satisfactorily with experimental results.

4.2. The effect of the orifice diameter

As mentioned above, both the visualized experiment and numerical calculations agree that the liquid strands are
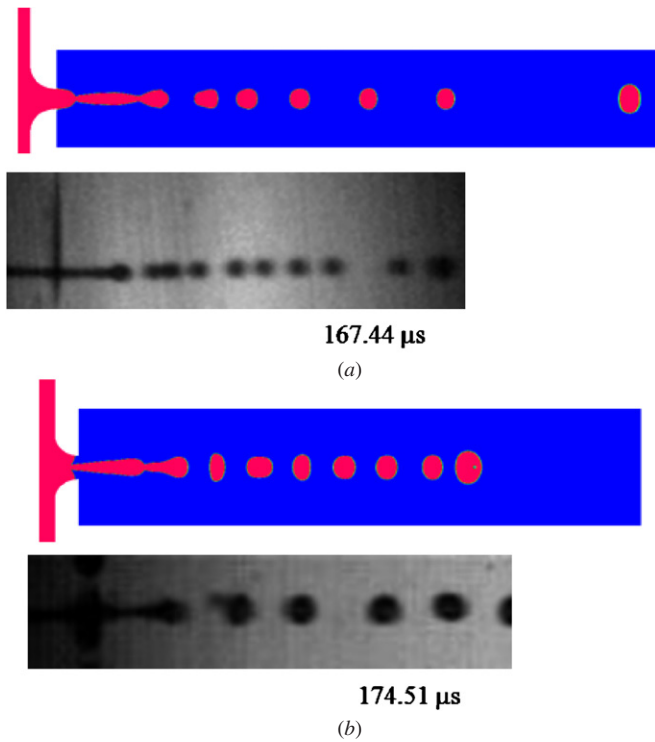
Figure 11. Comparison of the predicted and observed micro-images of the liquid shape: (*a*) case A and (*b*) case B.

discharged continuously under the validation conditions of our theoretical models given above. The tail of the ejecting drop would not detach from the remaining liquid portion inside the nozzle during the entire periodic vibration as shown in figure 12. A primary drop can be formed about every three periods of nozzle plate vibration through the destabilizing effect of surface tension. Fixed under the same conditions as the validation case except for the diameter of the orifice decreasing to 24 μm, the new liquid drop would overtake and coalesce into the previous one inside the nozzle after the beginning of the second periodic vibration as shown in figure 13.

When the diameter further decreased to 14 μm and 4 μm, the primary drop was formed and the remaining liquid column then disintegrated into a few small drops, so-called satellite drops during one periodic vibration, but, in the case of diameter 14 μm, the following liquid column induced by the new vibration moved more rapidly than the previous satellite decreased, thus causing coalescence of the liquid drops. Figure 14 illustrates the effect of the orifice diameter on the average drop velocity and volume.

The drop volume increased and velocity decreased with increasing diameter. In the uniformity analysis of the drop volume, the maximum difference between individual and average drop volumes attained 4.4% when the orifice diameter was 34 μm. In contrast, when the diameter decreased to 14 μm, the difference increased by 37%. On the basis of the limited data available, it is certain that when the diameter is equal to 34 μm, the satellite drops cannot occur because of a continuous liquid supplement into an ejected liquid column, and only the uniform primary drops become formed at the
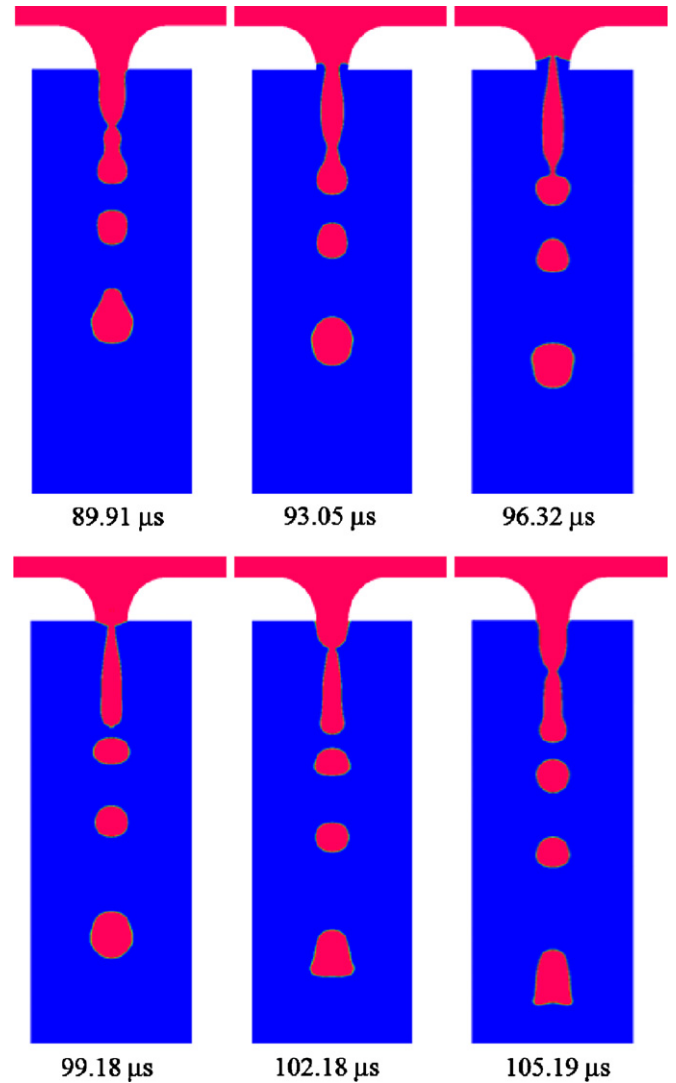

Figure 12. Temporal evolution of ejecting drops at a nozzle exit diameter of 34 μm.

leading edge. When the diameter was decreased to 14 μm, except for the formation of the primary drop at the leading edge, the liquid portions that follow tended to disintegrate into a few satellite drops, therefore causing a non-uniform drop volume. Excluding the orifice diameter, 14 μm, because of the occurrence of complicated coalescence of liquid drops and the first drop being inconsistent, the analysis of the period for disintegration of the drop shows that for the orifice diameter of 34 μm the breaking point occurred approximately at 77.43 μs whereas at 68.2 μs for a diameter of 24 μm. A possible reason might be that the momentum per volume for the diameter of 24 μm is greater than that for the diameter of 34 μm to overcome the restoring effects including viscosity and surface tension.

4.3. The effect of the curvature of the nozzle passage

To investigate the influence of the curvature of the nozzle passage on the drop formation, we devised six types of curvature, as shown in figure 15.
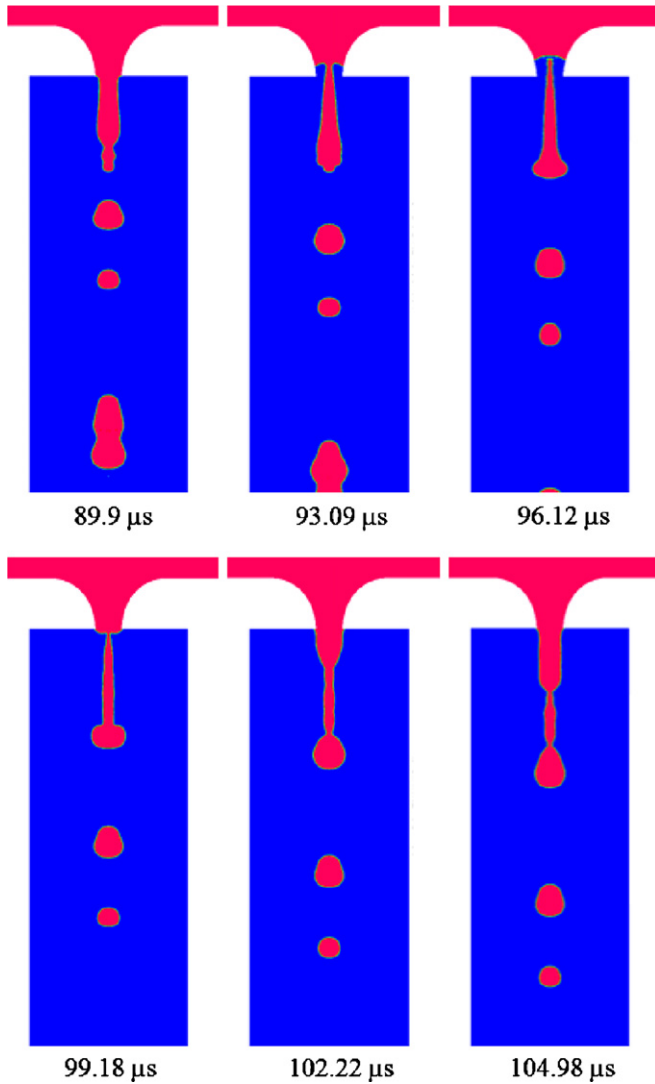
Figure 13. Temporal evolution of ejecting drops with a nozzle exit diameter of 24 μm.
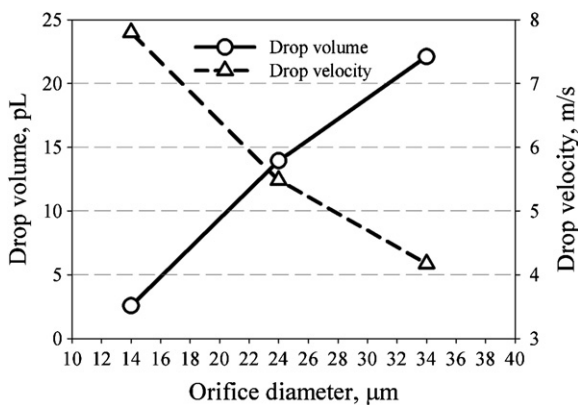

Figure 14. Effect of the diameter of the nozzle exit on the average drop velocity and volume.

The x axis coincides with the nozzle centerline and the y axis with the direction of the radius. All other parameters and configuration size information are presented in table 3.
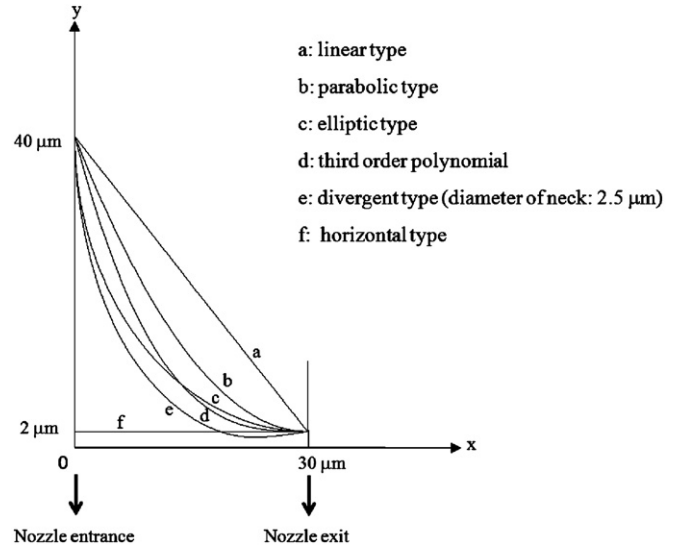

Figure 15. Types of nozzle passage curvature.

Table 3. Parameters and size information pertinent to types of passage curvature.

R_{out} (μm)	R_{in} (μm)	T (μm)	A (μm)	f (kHz)	θ_e (deg)
2	40	30	0.25, 1	100, 200	7.1

Figure 16 illustrates the effect of the passage curvature, vibrating amplitude and frequency on the average drop velocity.

The linear or uncurved type has the greatest drop velocity among all cases. When the vibrational amplitude and frequency increase from 0.25 μm to 1 μm and 100 kHz to 200 kHz, respectively, the drop velocity tends to increase. It is unlikely that a varied wall curvature contributed to the distinct distribution of liquid pressure and thus a pressure difference between the liquid and ambient air, the source of the forward momentum of liquid drops. Note that the velocity in the flow field of the linear type is as large as 845 m s^{-1} when the vibrational amplitude is 1 μm and 420 m s^{-1} when the frequency is 200 kHz. The Mach number, $M \equiv u/c$, where u is the speed of flow and c is the speed of sound, is comparable to the value 0.3. Therefore, the constant density assumption is invalid (Kundu and Cohen 2004). In other words, the present theoretical models fail to predict the droplet ejection process and dynamics in these cases. In addition, the method for estimating the average primary drop velocity is to measure the displacement of the leading edge of the droplet in a time period. According to the research (Dijksman 1984), the deceleration, β, of a drop with a radius r_d and speed v_d is

$$\beta = 4.577 \left(\frac{\rho_{air}^{2/5} \mu_{air}^{3/5}}{\rho_d} \right) \left(\frac{v_d^{7/5}}{r_d^{8/5}} \right), \qquad (17)$$

where ρ_{air} is the density of the surrounding air, ρ_d is the density of drops and μ_{air} is the viscosity of the air. For a drop with a radius of 2 μm and speed of about 100 m s^{-1}, the deceleration is around 1 μm μs^{-2}. In the current simulation, this decreasing velocity of the primary drop could be observed in the limit of
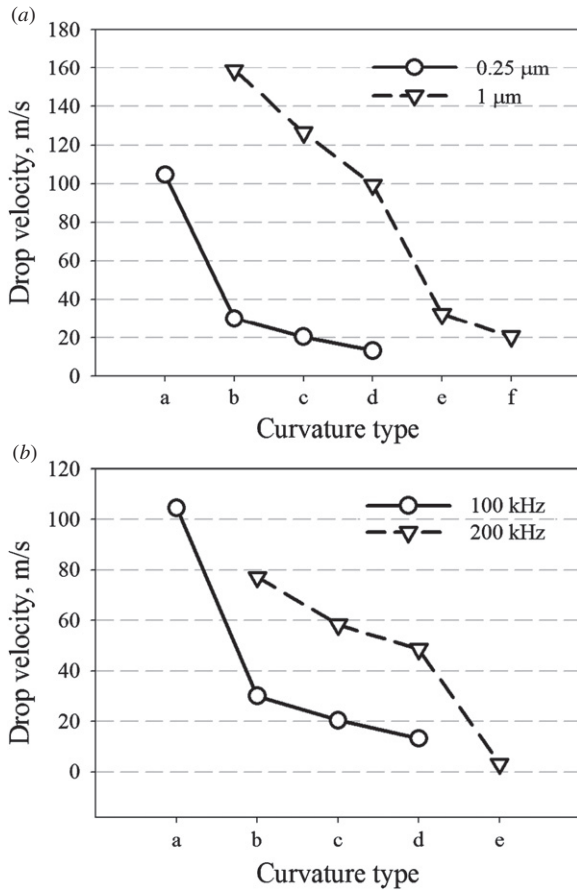
Figure 16. Effect of the curvature of the nozzle passage on the drop velocity, (*a*) varied amplitude with constant frequency 100 kHz and (*b*) varied frequency with constant amplitude 0.25 μm.
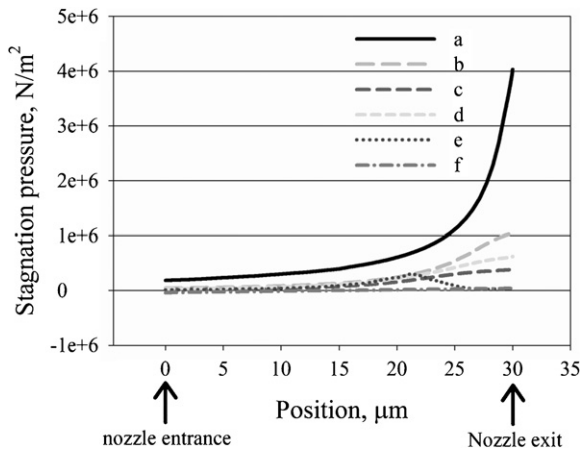

Figure 18. Effect of curvature of the nozzle wall on the primary drop volume, (*a*) varied amplitude with constant frequency 100 kHz and (*b*) varied frequency with constant amplitude 0.25 μm.

Figure 17. Magnitude of stagnation pressure of different curvature cases along the nozzle center line.

the solution domain. Shown in figure 17 is the magnitude of the stagnation pressure of different curvature cases along the nozzle center line when the vibrational amplitude and frequency are 0.25 μm and 100 kHz, respectively.

The overall pressure value in the linear case is greater than the others. The divergent and zero-curvature types might not expel the liquid column from the drops having insufficient
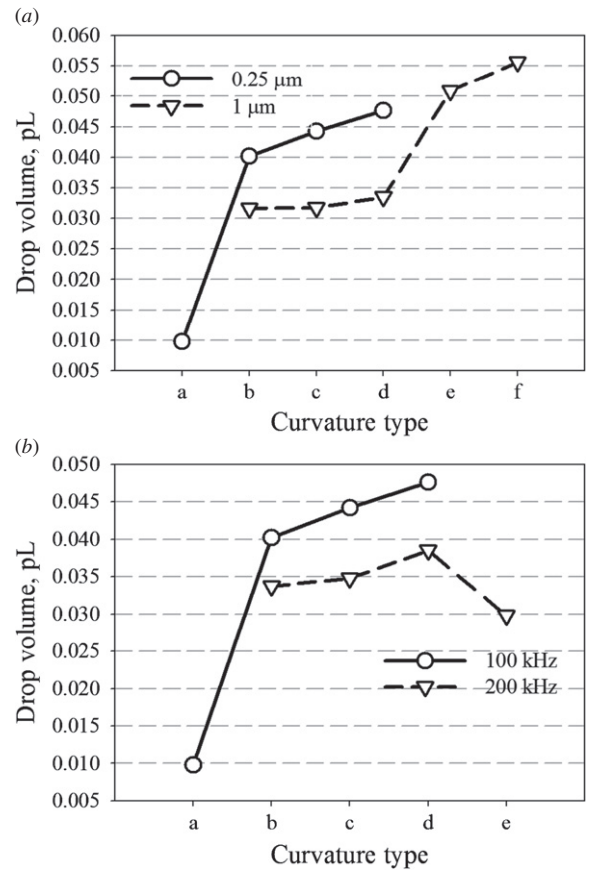
forward momentum. Figure 18 shows the effect of the wall curvature, the vibration amplitude and the frequency on the primary drop volume.

The linear-type curvature seems to produce the smallest drop volume among all cases with the same vibrational amplitude and frequency. Having a larger forward momentum per unit volume, the ejecting liquid column tended to be thinner and longer, thus causing smaller drops through the destabilizing effect of surface tension. When the vibrational amplitude was increased from 0.25 μm to 1 μm or the vibrational frequency from 100 kHz to 200 kHz, the volume difference for the parabolic type of curvature was the smallest among all curvatures. These results indicate that there is a diminishing return to a decreased drop volume on increasing the forward momentum imposed. The effect of the wall curvature, vibration amplitude and frequency on the duration of the formation of the primary drop is shown in figure 19.

The linear cases appeared to have the least time to disintegrate regardless of the amplitude and frequency.

4.4. The effect of the dynamic contact angle

The effects of the dynamic contact angle on the drop velocity, volume and duration of formation are shown in figures 20, 21 and 22, respectively. All other parameters and configuration size information are presented in table 4.
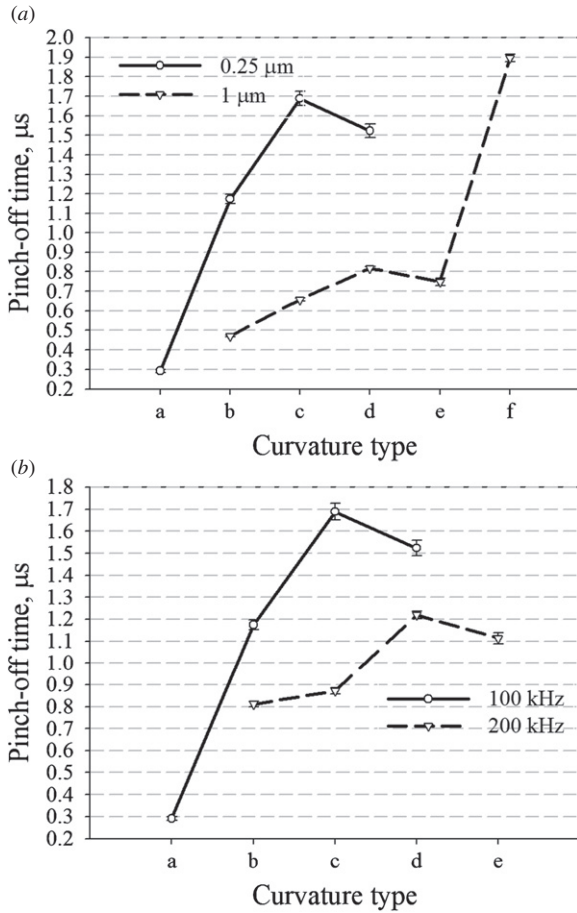
(*a*)

(*b*)

Figure 19. Effect of curvature of the nozzle wall on the drop pinching-off time, (*a*) varied amplitude with a constant frequency of 100 kHz and (*b*) varied frequency with a constant amplitude of 0.25 μm.
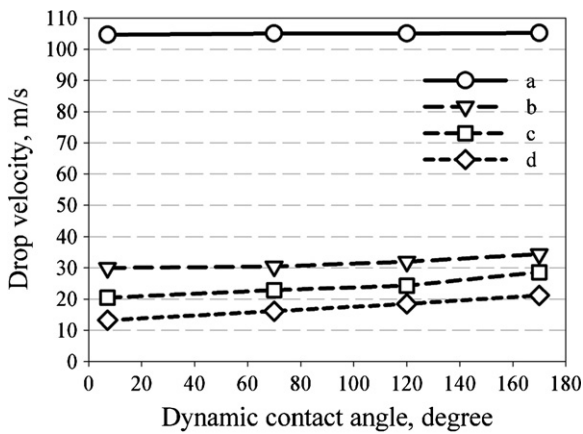

Figure 20. Effect of the dynamic contact angle on the drop velocity.

Table 4. Parameters and size information to investigate the effect of the contact angle.

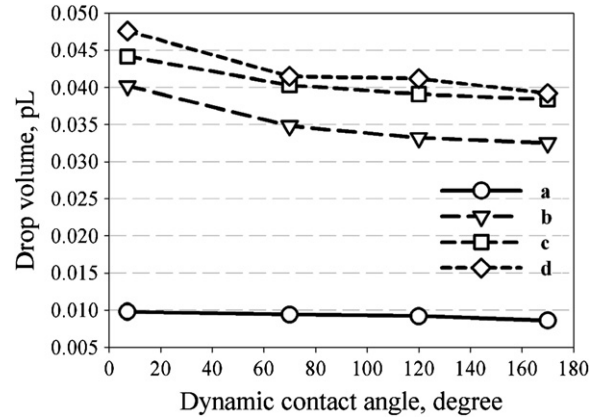| R_{out} (μm)	R_{in} (μm)	T (μm)	A (μm)	f (kHz)	θ_e (deg)
2	40	30	0.25	100	7.1, 70, 120, 170

Figure 21. Effect of the dynamic contact angle on the drop volume.
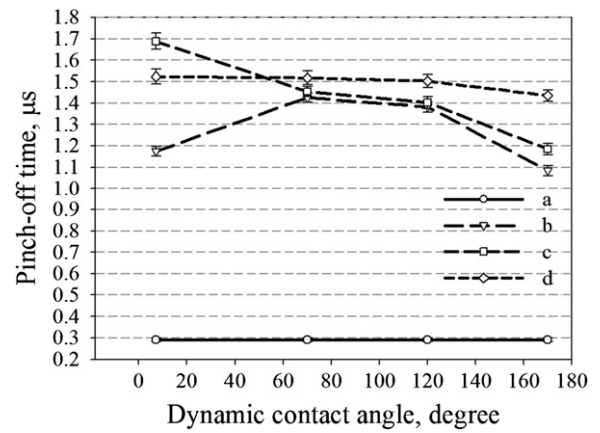

Figure 22. Effect of the dynamic contact angle on the drop pinching-off time.

The drop velocity increases for the contact angle increasing from 7.1° to 170°; the variation of the contact angle caused an effect on the difference between velocities as much as 0.54% in the linear case compared to a third-order case as much as 60%. The linear wall curvature might tend to have large momentum per unit volume in ejecting drops relative to the variable momentum caused by the effect of the contact angle. As shown in figure 21, a contact angle smaller than 70° causes an increased impact on the drop volume among all cases other than the linear-type case that appeared to decrease slightly. For the duration of the formation of the primary drop, the results reveal that this time is relatively small when the wetting condition of the nozzle wall is highly hydrophilic or hydrophobic except for the case of an elliptic-type curvature. Figure 23 illustrates the erratic change of the primary drop volume behind pinch-off when the dynamic contact angle is 70°. The difference between the maximum and minimum primary drop volume over a time period is within 1.5%. Based on the above results, numerical calculations have demonstrated that the effect of the wetting conditions on the droplet formation process has a significant difference among various types of curvature of the nozzle passage.
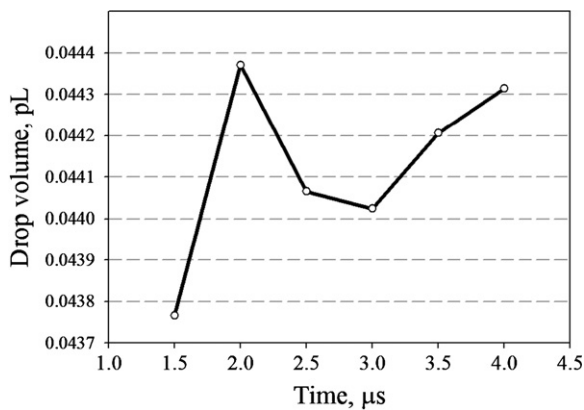
Figure 23. Variation with time of the primary drop volume behind pinch-off.

5. Conclusions

In this work, we have numerically investigated drop formation through a designed system of a nozzle plate connected with a flat-plate piezoelectric material. The major results are summarized as follows.

(1) Numerical and experimental results agree satisfactorily in the liquid shape. The discrepancy of the predicted and measured average drop velocity is 2.9%, while the drop volume is about 0.68%.

(2) When the diameter of the orifice equals 34 μm or 24 μm, the liquid strands seem to be expelled continuously and drops with uniform size distribution can be formed in the absence of satellite drops. In contrast, when the orifice diameter equals 14 μm or 4 μm, a primary drop with a few satellite drops is observed. The drop volume increased and average drop velocity decreased with increasing orifice diameter.

(3) Among varied curvatures of the nozzle wall, the linear type seems to have a larger drop velocity, a smaller drop volume and a smaller pinching-off period because of a larger pressure difference between water and ambient air.

(4) When the dynamic contact angle was altered from 7.1° to 170°, the drop velocity slightly increased and the volume decreased. The period to pinch off a drop tends to be relatively small when the contact angle is extremely large or small.

Acknowledgments

References

Allen R R, Meyer J D and Knight W R 1985 Thermodynamics and hydrodynamics of thermal ink jets *Hewlett-Packard J.* **36** 21–7

Anantharamaiah N, Tafreshi H V and Pourdeyhimi B 2006 Numerical simulation of the formation of constricted waterjets in hydroentangling nozzles—effects of nozzle geometry *Chem. Eng. Res. Des.* **84** 231–8

Anantharamaiah N, Tafreshi H V and Pourdeyhimi B 2007 A simple expression for predicting the inlet roundness of micro-nozzles *J. Micromech. Microeng.* **17** N31–N9

Asai A 1992 Three-dimensional calculation of bubble-growth and drop ejection in a bubble jet printer *Trans. ASME* I **114** 638–41

Asai A, Hara T and Endo I 1987 One-dimensional model of bubble-growth and liquid flow in bubble jet printers *Japan. J. Appl. Phys.* **1 26** 1794–801

Brackbill J U, Kothe D B and Zemach C 1992 A continuum method for modeling surface-tension *J. Comput. Phys.* **100** 335–54

Chen P H, Chen W C and Chang S H 1997 Bubble growth and ink ejection process of a thermal ink jet printhead *Int. J. Mech. Sci.* **39** 683–95

Chen P H, Peng H Y, Liu H Y, Chang S L, Wu T I and Cheng C H 1999 Pressure response and droplet ejection of a piezoelectric inkjet printhead *Int. J. Mech. Sci.* **41** 235–48

Chen S C, Cheng C H and Lin Y C 2005 Fabrication of components for a valve-less micropump or microejector by multilevel electroforming technology *6th Biennial Int. Workshop on High Aspect Ratio Micro Structure Technology* (Gyenogju, Korea: Springer) pp 455–63

Cheng C H, Chen S C and Chen Z S 2005 Multilevel electroforming for the components of a microdroplet ejector by UV LIGA technology *J. Micromech. Microeng.* **15** 843–8

Dijksman J F 1984 Hydrodynamics of small tubular pumps *J. Fluid Mech.* **139** 173–91

Dijksman J F and Pierik A 2008 Fluid dynamical analysis of the distribution of ink jet printed biomolecules in microarray substrates for genotyping applications *Biomicrofluidics* **2** 044101

Ehrfeld W 2002 Electrochemistry and microsystems *53rd Ann. Meeting of the Int. Soc. of Electrochemistry* (Dusseldorf, Germany: Pergamon-Elsevier Science) pp 2857–68

Fan K C, Chen J Y, Wang C H and Pan W C 2008 Development of a drop-on-demand droplet generator for one-drop-fill technology *Sensors Actuator* A **147** 649–55

Feng J Q 2002 A general fluid dynamic analysis of drop ejection in drop-on-demand ink jet devices *J. Imaging Sci. Technol.* **46** 398–408

Fromm J E 1984 Numerical calculation of the fluid dynamics of drop-on-demand jets *IBM J. Res. Dev.* **28** 322–33

Hirt C W and Nichols B D 1981 Volume of fluid (VOF) method for the dynamics of free boundaries *J. Comput. Phys.* **39** 201–25

Kim Y D, Kim J P, Kwon O S and Cho I H 2009 The synthesis and application of thermally stable dyes for ink-jet printed LCD color filters *Dyes Pigments* **81** 45–52

Komatsu M, Murayama Y and Hashimoto H 2008 Protein fragment imaging using ink jet printing digestion technique *Appl. Surf. Sci.* **255** 1162–4

Kothe D B, Rider W J, Mosso S J, Brock J S and Hochstein J I 1996 Volume tracking of interfaces having surface tension in two and three dimensions *AIAA* 96-0859

Kundu P K and Cohen I M 2004 *Fluid Mechanics* (San Diego: Elsevier Academic)

Kwon K S 2009 Speed measurement of ink droplet by using edge detection techniques *Measurement* **42** 44–50

Le H P 1998 Progress and trends in ink-jet printing technology *J. Imaging Sci. Technol.* **42** 49–62

Link N and Semiat R 2009 Ink drop motion in wide-format printers I. Drop flow from drop-on-demand (DOD) printing heads *Chem. Eng. Process.* **48** 68–83

Liou T M, Shih K C, Chau S W and Chen S C 2002 Three-dimensional simulations of the droplet formation during the inkjet printing process *Int. Commun. Heat Mass Transf.* **29** 1109–18

Meinhart C D and Zhang H S 2000 The flow structure inside a microfabricated inkjet printhead *J. Microelectromech. Syst.* **9** 67–75

Moon K S, Choi J H, Choi D J, Kim S H, Ha M H, Nam H J and Kim M S 2008 A new method for analyzing the refill process and fabrication of a piezoelectric inkjet printing head for LCD color filter manufacturing *J. Micromech. Microeng.* **18** 13

Pan F X, Kubby J and Chen J K 2002 Numerical simulation of fluid–structure interaction in a MEMS diaphragm drop ejector *J. Micromech. Microeng.* **12** 70–6

Pimbley W T 1976 Drop formation from a liquid jet: a linear one-dimensional analysis considered as a boundary value problem *IBM J. Res. Dev.* **20** 148–56

Pond S F 2000 *Inkjet Technology and Product Development Strategies* (Carlsbad: Torrey Pines Research)

Rayleigh L 1878 On the stability of liquid jets *Proc. London Math. Soc.* **10** 4

Rider W J and Kothe D B 1998 Reconstructing volume tracking *J. Comput. Phys.* **141** 112–52

Ridley B A, Nivi B and Jacobson J M 1999 All-inorganic field effect transistors fabricated by printing *Science* **286** 746–9

Shield T W, Bogy D B and Talke F E 1987 Drop formation by DOD ink-jet nozzles—a comparison of experiment and numerical-simulation *IBM J. Res. Dev.* **31** 96–110

Shimoda T, Morii K, Seki S and Kiguchi H 2003 Inkjet printing of light-emitting polymer displays *MRS Bull.* **28** 821–7

Suh Y and Son G 2008 A level-set method for simulation of a thermal inkjet process *Numer. Heat Transfer* B **54** 138–56

Wu H C, Hwang W S and Lin H J 2004 Development of a three-dimensional simulation system for micro-inkjet and its experimental verification *Mater. Sci. Eng.* A **373** 268–78

Yang A S, Yang J C and Hong M C 2006 Droplet ejection study of a Picojet printhead *J. Micromech. Microeng.* **16** 180–8

Yu J D, Sakai S and Sethian J 2005 A coupled quadrilateral grid level set projection method applied to ink jet simulation *J. Comput. Phys.* **206** 227–51